Monthly Notices of the ROYAL ASTRONOMICAL SOCIETY

MNRAS **530,** 4887–4901 (2024) https://doi.org/10.1093/mnras/stae405
Advance Access publication 2024 February 8

Little evolution of dust emissivity in bright infrared galaxies from $2 < z < 6$

B. A. Ward,[1]★ S. A. Eales,[1] R. J. Ivison [2,3,4,5] and V. Arumugam[6]

[1]*Cardiff Hub for Astrophysics Research and Technology (CHART), School of Physics and Astronomy, Cardiff University, The Parade, Cardiff CF24 3AA, UK*
[2]*European Southern Observatory (ESO), Karl-Schwarzschild-Strasse 2, D-85748 Garching, Germany*
[3]*ARC Centre of Excellence for All Sky Astrophysics in 3 Dimensions (ASTRO 3D)*
[4]*School of Cosmic Physics, Dublin Institute for Advanced Studies, 31 Fitzwilliam Place, Dublin D02 XF86, Ireland*
[5]*Institute for Astronomy, University of Edinburgh, Royal Observatory, Blackford Hill, Edinburgh EH9 3HJ, UK*
[6]*Institut de Radioastronomie Millimétrique, Domaine Universitaire, 300 rue de la Piscine, F-38406 Saint Martin d'Hères, France*

Accepted 2024 January 19. Received 2024 January 13; in original form 2023 October 26

ABSTRACT

Variations in the dust emissivity index, β, within and between galaxies, are evidence that the chemistry and physics of dust must vary on large scales, although the nature of the physical and/or chemical variations is still unknown. In this paper, we estimate values of β and dust temperature for a sample of 109 dusty star-forming galaxies (DSFGs) over the range, $2 < z < 6$. We compare the results obtained with both an optically thin model and a general opacity model, finding that our estimates of β are similar between the models but our estimates of dust temperature are not. We find no evidence of a change in β with redshift, with a median value of $\beta = 1.96$ for the optically thin model with a confidence interval (16–84 per cent) of 1.67 to 2.35 for the population. Using simulations, we estimate the measurement errors from our procedure and show that the variation of β in the population results from intrinsic variations in the properties of the dust in DSFGs. At a fixed far-infrared luminosity, we find no evidence for a change in dust temperature, $T_{\rm dust}$, with redshift. After allowing for the effects of correlated measurement errors, we find an inverse correlation between β and $T_{\rm dust}$ in DSFGs, for which there is also evidence in low-redshift galaxies.

Key words: galaxies: evolution – submillimetre: galaxies.

1 INTRODUCTION

Despite contributing only a small percentage ($\lesssim$1 per cent) of the mass of the interstellar medium (Galliano, Galametz & Jones 2018), interstellar dust plays a pivotal role in the star formation processes of galaxies. Dust efficiently absorbs optical and ultraviolet light from young OB-type stars and active galactic nuclei (AGNs) and re-emits this radiation at longer wavelengths, in the far-infrared (FIR) to millimetre-wave (mm) regimes (e.g. Puget et al. 1996; Dwek et al. 1998; Fixsen et al. 1998; Dole et al. 2006; Driver et al. 2008). This dust obscuration hides star formation activity in the most massive, dust-enshrouded galaxies in the early Universe. The most intense star formation occurs in dusty star-forming galaxies (DSFGs) at high redshifts ($z > 1$) where stars were produced at rates of $\gtrsim$100–1000 $\mathrm{M_\odot\,yr^{-1}}$, causing high infrared luminosities ($L_{\rm IR}$), often in excess of $\sim 10^{12}\,\mathrm{L_\odot}$ (Blain et al. 2002; Casey, Narayanan & Cooray 2014; Swinbank et al. 2014; da Cunha et al. 2015, 2021; Dudzevičiūtė et al. 2020).

The first high-redshift DSFGs were discovered using the Submillimetre Common User Bolometer Array (SCUBA; Holland et al. 1999) on the 15-m James Clerk Maxwell Telescope (JCMT) at 850 μm (Smail, Ivison & Blain 1997; Barger et al. 1998; Hughes et al. 1998; Eales et al. 1999). Since their discovery, many samples have been selected at wavelengths between 450 μm to 2 mm using SCUBA's successor, SCUBA-2 (Holland et al. 2013), e.g. by Wang et al. (2017) and Dudzevičiūtė et al. (2020), and by other single-dish FIR–mm facilities such as the *Herschel Space Observatory* (e.g. Eales et al. 2010; Oliver et al. 2012), AzTEC (e.g. Montaña et al. 2021), and the South Pole Telescope (SPT; e.g. Vieira et al. 2010; Everett et al. 2020), aided by the negative K correction, which means that flux densities decline very slowly for a fixed $L_{\rm IR}$ at $z > 1$ (e.g. Blain & Longair 1993).

The very large star formation rates in these galaxies suggest they contain very large masses of molecular gas. Since it is impossible to observe the molecular hydrogen directly, the mass of molecular gas in the DSFGs has been estimated by the standard method of making observations of a 'tracer' of the hidden gas, then estimating the gas mass from the luminosity of the tracer and a calibration factor linking the two. The tracers that have been used are the CO molecule, dust grains, and carbon atoms (e.g. Dunne et al. 2022). The dust method (e.g. Eales et al. 2012; Magdis et al. 2012; Scoville et al. 2014) is particularly useful for DSFGs because they are powerful sources of thermal continuum emission. Studies of the DSFGs and other high-redshift galaxies have shown that they contain a higher fraction of gas than observed in galaxies today (e.g. Tacconi et al. 2010; Scoville et al. 2016, 2017; Millard et al. 2020).

In considering this result, however, it should be remembered that the calibration factors are ultimately based on observations in our own Galaxy, and therefore the method is based on the

★ E-mail: WardB2@cardiff.ac.uk

implicit assumption that the physics and other properties of the tracer do not evolve with redshift. In the case of the dust method, this boils down to the assumptions that the gas-to-dust ratio and the physical and chemical properties of the dust do not change with redshift. Recent observational (e.g. Shapley et al. 2020; Popping & Péroux 2022) and theoretical (e.g. Popping, Somerville & Galametz 2017; Li, Narayanan & Davé 2019) studies have concluded that the dust-to-gas ratio does not appear to evolve with redshift.

One useful observational indicator of the physical and chemical properties of the dust grains is the dust emissivity spectral index, β, which describes the frequency dependence of the emissivity of the dust grains, with the optical depth of the dust being approximated as a power law, $\tau \propto \nu^{\beta}$. Theoretical models of dust (e.g. Draine & Lee 1984) predict that β should range between 1 and 2 depending on the chemical composition of the dust grains. The value for dust in the Galaxy is remarkably uniform over the sky, with a value of $\beta = 1.51 \pm 0.01$ (Planck Collaboration XXII 2015). Although the assumption necessary to use dust as a tracer of the hidden molecular hydrogen is that the properties of dust are the same in every galaxy, there is now plenty of evidence that this is not true. For example, Lamperti et al. (2019) modelled the FIR spectral energy densities (SEDs) of 192 nearby galaxies from JINGLES (the JCMT dust and gas In Nearby Galaxies Legacy Exploration Survey) and found β values between 0.6 and 2.2. Also, there is now evidence for radial variation of β within galaxies (e.g. Smith et al. 2012; Draine et al. 2014; Tabatabaei et al. 2014; Hunt et al. 2015; Whitworth et al. 2019; Clark et al. 2023).

In this study, we test the assumption that the properties of dust are the same at all cosmic epochs by investigating whether there is evidence for evolution in the value of the dust emissivity index. We study bright FIR sources detected by *Herschel* and SPT with spectroscopically determined redshifts between $2 \lesssim z_{\rm spec} \lesssim 6$, and model their FIR dust emission to determine the value of β for each galaxy. We investigate whether there is any difference between these values and those in galaxies today, and also whether there is any change over this redshift range, corresponding to the period between about a billion years after the big bang and the epoch at which cosmic star formation was at its peak (e.g. Lilly et al. 1996).

The paper is organized as follows. In Section 2, we describe the sample used during this analysis. In Section 3, we derive the dust properties of our sources by fitting their SEDs with modified blackbodies. In Section 4, we consider the impact of the well-studied β–dust temperature degeneracy and the extent to which this biases our results. We also discuss the robustness of our estimated dust parameters by presenting simple simulations that imitate the SED fitting routine on mock *Herschel* and SPT sources. Section 5 describes the results of our analysis and the suite of simulations used to predict the accuracy of our estimated dust properties. We also discuss the implications of our findings in the context of the existing literature for low-redshift galaxies. Finally, we provide a summary of our results in Section 6. Throughout this paper, we assume a lambda cold dark matter cosmology with $H_0 = 67.7\,{\rm km\,s^{-1}\,Mpc^{-1}}$ and $\Omega_{\rm m} = 0.31$ (Planck Collaboration VI 2020).

2 THE SAMPLE

The sample studied here is a combination of DSFGs from *Herschel*, specifically from HerBS (*Herschel* Bright Sources; Bakx et al. 2018), and from the SPT (Reuter et al. 2020).

2.1 HerBS subsample

The first subsample used in this study comes from the HerBS catalogue, a selection of the brightest high-redshift sources detected during the *Herschel*-Astrophysical Terahertz Large Area Survey (*H*-ATLAS; Eales et al. 2010). The sample contains 209 galaxies with 500 μm flux densities above 80 mJy and photometric redshift estimates in excess of 2.

Spectroscopic redshifts have been obtained for a selection of HerBS sources within the South Galactic Pole field of *H*-ATLAS, as part of the Bright Extragalactic ALMA Redshift Survey (BEARS; Urquhart et al. 2022; Bendo et al. 2023; Hagimoto et al. 2023). These redshifts were measured from CO spectral lines detected with the band-3 receivers of the Atacama Compact Array, which is part of the Atacama Large Millimetre Array (ALMA), and also from spectral lines detected with the band-3 and band-4 receivers of ALMA's 12-m array. The high spatial resolution of the ALMA band-4 images (∼2 arcsec) revealed that many HerBS sources are composed of more than one source; only half of the HerBS sources comprise a single source at ALMA's spatial resolution. In total, Urquhart et al. (2022) measured 71 spectroscopic redshifts for 62 entries in the HerBS catalogue. Several HerBS sources comprise two or more ALMA sources with spectroscopic redshifts that agree well, suggesting either that the sources are physically associated galaxies or are multiple images caused by gravitational lensing. For this study, we have retained the HerBS sources which are multiples in the ALMA images, if the redshifts of the sources are within 0.1 of each other (we have taken the average redshift as that of the system). If there are multiple sources in the ALMA image within the *Herschel* beam but a spectroscopic redshift for only one source, we have assumed the sources are physically connected and used the redshift of the one source as the redshift of the system.

In our study, we have used all HerBS sources with spectroscopic redshifts and photometry at 250, 350, and 500 μm (*Herschel*-SPIRE), at 850 μm (Bakx et al. 2018) and at 2 and 3 mm from ALMA (Bendo et al. 2023). We have also used photometry in ALMA band-6 (1.1–1.4 mm) from the ALMARED survey (Chen et al. in preparation) of potentially 'ultrared' (see Ivison et al. 2016) sources in *H*-ATLAS (project code 2018.1.00526.S). The minimum and maximum redshifts are $z_{\rm min} = 1.569$ and $z_{\rm max} = 4.509$.

2.2 SPT subsample

Our second subsample comprises the 81 DSFGs selected using the SPT (Weiß et al. 2013; Strandet et al. 2016; Reuter et al. 2020). For a source to be included in this subsample, it must have a flux density above 25 mJy at 870 μm. Redshifts for all SPT sources were obtained via blind searches targeting CO line emission (Weiß et al. 2013; Strandet et al. 2016; Reuter et al. 2020). There are robust spectroscopic redshifts (from two or more CO lines) for all except two sources. We have retained the two because their spectroscopic redshifts are consistent with the redshifts estimated from photometry. The subsample has redshifts over the range $1.867 < z_{\rm spec} < 6.901$ and a median redshift of 3.9 ± 0.2 (Reuter et al. 2020). The SPT redshift distribution extends to higher redshifts than that of HerBS because the longer selection wavelength modifies the effect of the negative *K* correction. The extreme apparent luminosities of the SPT sources implies that most of them are gravitationally lensed, with lensing models based on ALMA observations giving a median lensing magnification factor of 5.5× (Spilker et al. 2016).

The SPT sources have photometry between 250 μm and 3 mm, corresponding to a rest-frame range of $86\,\mu{\rm m} \lesssim \lambda_{\rm rest} \lesssim 380\,\mu{\rm m}$,

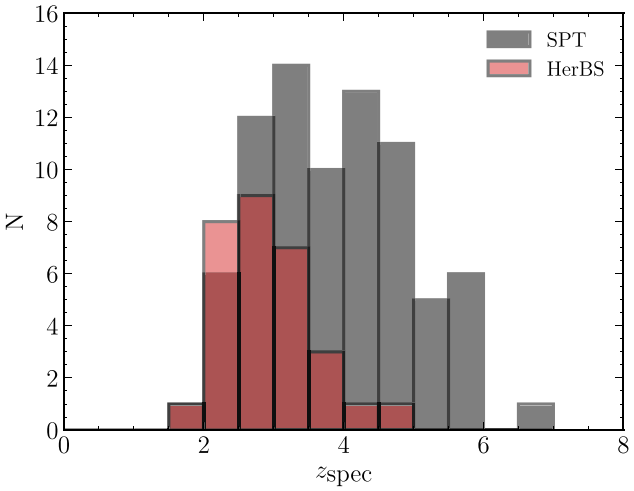

Figure 1. Spectroscopic redshift distributions for the SPT DSFGs (grey) and those from HerBS/BEARS (red).

meaning that the peak of the dust emission (∼100 μm) and Rayleigh–Jeans (R–J) tail are well sampled. The photometry includes flux densities measured at 250, 350, and 500 μm (*Herschel*-SPIRE), at 870 μm (APEX-LABOCA), at 1.4 and 2 mm (SPT) and at 3 mm (ALMA). For 65 sources, there are additional constraints at 100 and 160 μm from *Herschel*-PACS.

2.3 Restrictions on sample for this study

The two subsamples contain 143 galaxies with spectroscopic redshifts. However, as we are interested in estimating the galaxy-integrated β of each source, which is characterized by the slope of the dust emission on the R–J side of the Planck function, we restrict our final sample to those galaxies that have at least two photometric measurements at observed wavelengths beyond 1 mm. This reduces our sample to a total of 109 galaxies (79 SPT DSFGs, plus 30 from HerBS/BEARS). While the fitting methods used in this work are the same for both subsamples, we treat the two separately to look for effects that might have been caused by their different selection wavelengths and flux density limits. In Fig. 1, we show the redshift distributions of the two subsamples. The photometry and redshifts of the HerBS–BEARS sources are tabulated in Appendix A1; the corresponding data used in this work for the SPT sources can be found in Reuter et al. (2020).

3 SED FITTING

We model the FIR-to-millimetre spectra of our galaxies with a single modified blackbody (MBB) model combined with a mid-IR power law, where the MBB represents the emission from the reservoir of cold dust, which represents most of the dust in the ISM, and the power law represents emission from any dust in the vicinity of star-forming regions, young OB stars, or AGNs. The observed flux density can be expressed in the following form:

$$S_{\nu,\rm obs} = \begin{cases} \frac{\Omega}{(1+z)^3}(1-{\rm e}^{-\tau_\nu})B_\nu(T_{\rm dust}), & \nu \le \nu_{\rm c} \\ N\nu^{-\alpha}, & \nu > \nu_{\rm c} \end{cases}, \quad (1)$$

where Ω represents the solid angle subtended by the galaxy, τ_ν is the dust optical depth, $B_\nu(T_{\rm dust})$ is the Planck function assuming a characteristic dust temperature of the dust grains, $T_{\rm dust}$, N is a normalization for the power law that is tied to the normalization of the blackbody, and α is the mid-IR power-law index. The value of $\nu_{\rm c}$ is the frequency at which the gradient of the MBB is equal to the value of α.

We define the solid angle, Ω, as $\frac{A(1+z)^4}{D_{\rm L}^2}$, where A is the area of the source and $D_{\rm L}$ represents the luminosity distance. The optical depth, τ_ν, is defined as the product of dust surface mass density, $\Sigma_{\rm dust} = M_{\rm dust}/A$, and the dust opacity, κ_ν, but is often assumed to take the form of a power law, $(\nu/\nu_1)^\beta$, where ν_1 represents the frequency at which the optical depth equals unity, marking the frequency of the transition between optically thin and optically thick dust. This parameter can be reformulated in terms of intrinsic properties by equating the two forms of τ such that $\nu_1 = \nu_0(\kappa_0\Sigma_{\rm dust})^\beta$. In a similar fashion, κ_ν may be assumed to take a power-law form: $\kappa_\nu = \kappa_0(\nu/\nu_0)^\beta$, where κ_0 is the emissivity of the dust grains per unit mass at a given reference frequency, ν_0. In the following, we assume $\kappa_0 = 0.077\,{\rm m^2\,kg^{-1}}$ at $\nu_0 = 353\,{\rm GHz}$ (Dunne et al. 2000; James et al. 2002). Combining these, we find the following equation for the observed flux density of a galaxy:

$$S_{\nu,\rm obs} = \begin{cases} \frac{\mu A(1+z)}{D_{\rm L}^2}\left(1-{\rm e}^{-\frac{M_{\rm dust}\kappa_\nu}{A}}\right)B_\nu(T_{\rm dust}), & \nu \le \nu_{\rm c} \\ \mu N\nu^{-\alpha}, & \nu > \nu_{\rm c} \end{cases}, \quad (2)$$

where we have included a term, μ, to account for the possibility of magnification due to gravitational lensing. For sources where there is no evidence of gravitational lensing, we assume $\mu = 1$.

As demonstrated by da Cunha et al. (2013), the heating of dust by the cosmic microwave background (CMB) has a non-negligible effect on the shape of the FIR SED when the temperature of the CMB is a significant fraction of the dust temperature of a galaxy (see also Zhang et al. 2016 for the influence of the CMB on the measurement of structural and dynamical properties). Including the effects of the CMB on the observed dust continuum using the procedure outlined in da Cunha et al. (2013), the CMB-adjusted MBB model is now given by

$$S_{\nu,\rm obs} = \begin{cases} f_{\rm CMB}\frac{\mu A(1+z)}{D_{\rm L}^2}\left(1-{\rm e}^{-\frac{M_{\rm dust}\kappa_\nu}{A}}\right)B_\nu(T_{\rm dust}(z)), & \nu \le \nu_{\rm c} \\ f_{\rm CMB}\mu N\nu^{-\alpha}, & \nu > \nu_{\rm c} \end{cases}, \quad (3)$$

where we have made the following two changes: (i) the prefactor, $f_{\rm CMB}$, denotes the fraction of the total dust emission that is observed against the background caused by the hotter CMB at higher redshifts, given by equation (18) of da Cunha et al. (2013), i.e. $f_{\rm CMB} = \frac{S_\nu^{\rm observed}}{S_\nu^{\rm intrinsic}} = 1 - \frac{B_\nu[T_{\rm CMB}(z)]}{B_\nu[T_{\rm dust}(z)]}$ and (ii) we have re-defined the dust temperature to be a function of redshift due to the influence on dust grains of the warmer CMB at higher redshifts. The derived dust temperature is corrected for CMB effects using equation (12) of da Cunha et al. (2013), i.e. $T_{\rm dust}(z) = [T_{\rm dust,0}^{4+\beta} + T_{\rm CMB,0}^{4+\beta}((1+z)^{4+\beta}-1)]^{\frac{1}{4+\beta}}$, where $T_{\rm dust,0}$ is the dust temperature as observed at $z = 0$ and $T_{\rm CMB,0} = 2.73\,{\rm K}$ is the CMB temperature at $z = 0$. Note that all further mention of the dust temperature refers to the CMB-corrected, luminosity-weighted dust temperature as given by the model described above, unless otherwise stated. Using this general form of the MBB, there are up to four free parameters: the dust mass, the dust temperature, $T_{\rm dust}$, the dust emissivity index, β, and the frequency at which the dust opacity reaches unity. If the physical area of the region emitting the submillimetre emission is known, the opacity can be calculated from the surface density of the dust.

We estimated the parameters of the dust using three different models. In the first model, we assume the dust is optically thin at all wavelengths ($\tau_\nu \ll 1$), which eliminates the fourth of the free

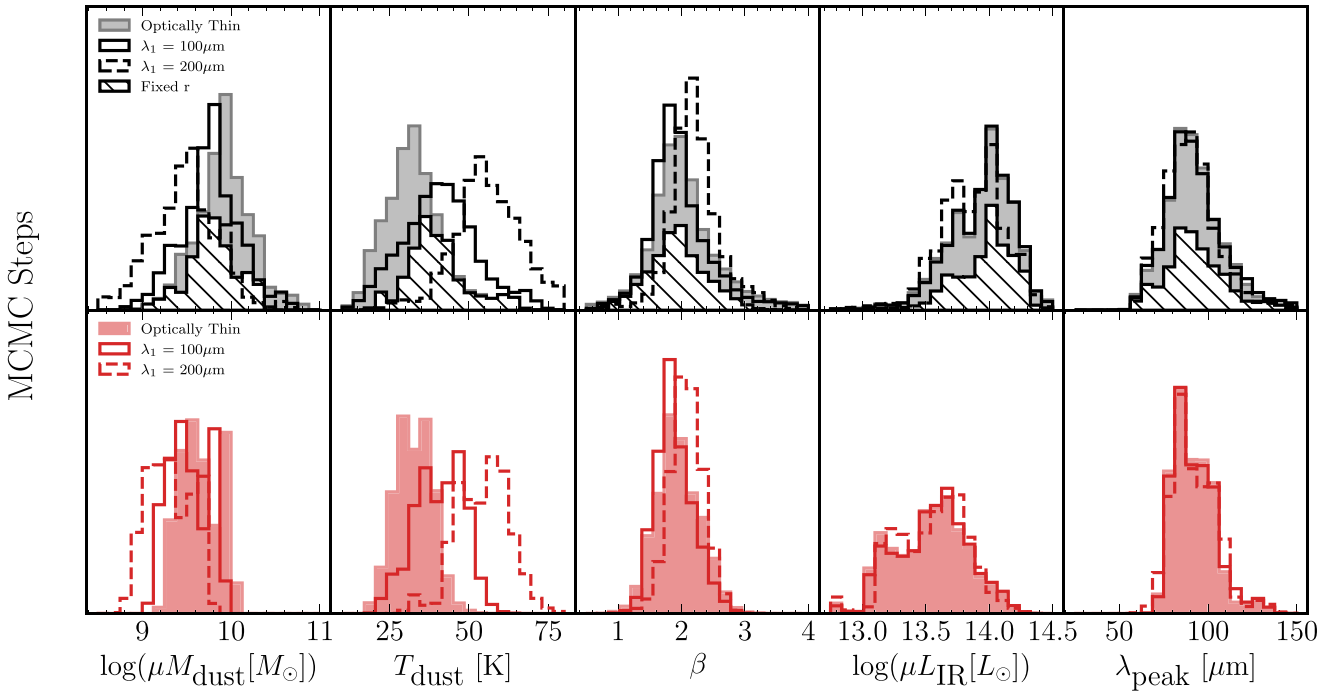

Figure 2. Stacked posterior distributions of $\log(\mu M_{\rm dust})$, $T_{\rm dust}$, β, $\log(\mu L_{\rm IR})$ (rest frame 8–1000 μm), and $\lambda_{\rm peak}$ for SPT (top panels) and HerBS galaxies (bottom panels). The posterior distribution for each MBB model is illustrated as follows: optically thin (shaded); $\lambda_1 = 100$ μm (solid line); $\lambda_1 = 200$ μm (dashed line); fixed continuum size (hatched).

parameters in the list above and modifies equation (3) to

$$S_{\nu,\rm obs} = \begin{cases} f_{\rm CMB}\frac{\mu(1+z)}{D_{\rm L}^2} M_{\rm dust}\kappa_\nu B_\nu(T_{\rm dust}(z)), & \nu \le \nu_{\rm c} \\ f_{\rm CMB}\mu N \nu^{-\alpha}, & \nu > \nu_{\rm c} \end{cases}. \quad (4)$$

However, since in DSFGs a large amount of dust is packed into a small region (e.g. Ikarashi et al. 2017), it is possible that the dust is optically thick at one or more of the wavelengths covered by our photometry (e.g. Conley et al. 2011; Casey et al. 2019; Cortzen et al. 2020). We therefore also used two models in which the dust becomes optically thick at wavelengths below $\lambda_1 = 100$ or 200 μm.

Some of the SPT sources have measurements of the sizes of the submillimetre-emitting region, typically ∼1 kpc (Spilker et al. 2016). For this subset of sources, we also fitted a modified MBB using the size of the emitting region to calculate the opacity directly.

To estimate the mass and luminosity of the dust, we require an estimate of the lensing magnifications, which we have taken to be those quoted in the lens modelling of Spilker et al. (2016) for the SPT sources and from the correlation between CO luminosity and line width as determined by Urquhart et al. (2022) for HerBS, building on the work of Harris et al. (2012). During SED fitting, we assume flat priors on all free parameters and take the best-fitting SED to be the median value of the posterior distribution for each parameter. The (1σ) uncertainties are quoted at the 16th and 84th percentiles. We present examples of the obtained posterior distributions in Appendix C1 . Calibration errors are added in quadrature with the flux density uncertainties assuming absolute calibrations of 7 per cent (*Herschel*-PACS), 5.5 per cent (*Herschel*-SPIRE), 5 per cent (SCUBA-2), 12 per cent (APEX-LABOCA), 7 per cent (SPT), and 10 per cent (ALMA).

Table 1. Median and 1σ errors, estimated from the 16th, 50th, and 84th percentiles of the stacked posterior distribution, for the parameters presented in Fig. 2.

Parameter	Optically thin	$\lambda_1 =$ 100 μm	$\lambda_1 =$ 200 μm
		SPT	
$\log[\mu M_{\rm dust}(M_\odot)]$	$9.92^{+0.30}_{-0.31}$	$9.77^{+0.31}_{-0.34}$	$9.49^{+0.37}_{-0.41}$
$T_{\rm dust}$ (K)	$32.07^{+8.43}_{-8.44}$	$40.77^{+10.90}_{-11.77}$	$55.63^{+11.20}_{-9.28}$
β	$1.98^{+0.54}_{-0.39}$	$1.91^{+0.50}_{-0.32}$	$2.18^{+0.38}_{-0.30}$
$\log[\mu L_{\rm IR}(L_\odot)]$	$13.98^{+0.19}_{-0.31}$	$13.99^{+0.19}_{-0.30}$	$13.89^{+0.23}_{-0.27}$
$\lambda_{\rm peak}$ (μm)	$90.70^{+17.33}_{-12.72}$	$90.70^{+18.36}_{-13.02}$	$89.28^{+15.21}_{-13.39}$
		HerBS	
$\log[\mu M_{\rm dust}(M_\odot)]$	$9.62^{+0.30}_{-0.22}$	$9.49^{+0.31}_{-0.22}$	$9.30^{+0.33}_{-0.26}$
$T_{\rm dust}$ (K)	$32.73^{+5.85}_{-5.92}$	$41.16^{+7.48}_{-8.20}$	$55.18^{+7.25}_{-9.23}$
β	$1.92^{+0.39}_{-0.32}$	$1.85^{+0.34}_{-0.25}$	$2.08^{+0.26}_{-0.25}$
$\log[\mu L_{\rm IR}(L_\odot)]$	$13.55^{+0.27}_{-0.37}$	$13.57^{+0.26}_{-0.37}$	$13.57^{+0.25}_{-0.34}$
$\lambda_{\rm peak}$ (μm)	$90.03^{+12.70}_{-9.28}$	$90.36^{+13.42}_{-9.46}$	$89.96^{+14.92}_{-9.46}$

4 RESULTS

4.1 Comparison between the optically thin and general opacity models

Fig. 2 shows the stacked posterior probability distributions for the dust parameters derived for the two samples. The median values and the 16th and 84th percentiles of the probability distributions are listed in Table 1. The median value of the main parameter of interest, the dust emissivity spectral index, covers only a range of 0.2 for the three models, showing that it does not make much difference what one assumes about the opacity, a conclusion also reached in

a study of a different sample of DSFGs by Ismail et al. (2023). We note, however, that the general opacity model with the highest value of λ_1 does give the highest value of β, as observed previously by McKay et al. (2023). Using a sample of 870 μm-selected galaxies in GOODS-S, McKay et al. (2023) found good agreement in the median β between an optically thin model (1.78) and an MBB model with $\lambda_1 = 100$ μm (1.80), but this increased to 2.02 for a model with $\lambda_1 = 200$ μm. Some recent studies have suggested that $\beta > 2$ is common among high-redshift galaxies (Casey et al. 2019, 2021; Cooper et al. 2022), but this may be due to these studies using a higher value for the wavelength at which the dust becomes optically thick.

The assumption that the dust is optically thin does, however, have a much larger effect for some of the other parameters. There is a clear trend to higher median dust temperatures with increasing λ_1, with increases of ∼10 and ∼20 K from the optically thin model to the $\lambda_1 = 100$ μm and to the $\lambda_1 = 200$ μm general opacity models, respectively. The dust masses decrease by approximately 0.1 $\log(\mu M_\odot)$ and 0.4 $\log(\mu M_\odot)$ from the optically-thin model to the $\lambda_1 = 100$ μm and the $\lambda_1 = 200$ μm general opacity models, respectively, though we note that these decreases are smaller than the 1σ widths of the probability distributions. There is no significant difference in IR luminosities or peak wavelengths between the models.

Fig. 2 also shows the posterior probability distributions for the subset of SPT galaxies for which we are able to estimate the area of the dust region (hatched histograms). This distribution agrees well with the probability distributions for the optically thin model and for the general-opacity model with $\lambda_1 = 100$ μm, but not for the one with $\lambda_1 = 200$ μm. For this subset of galaxies we find a median value of $\lambda_1 = 88$ μm (16th and 84th percentile range 44–224 μm). However, we note that this value is inversely proportional to the value assumed for the dust opacity (κ_ν) and since the opacity of interstellar dust is still very uncertain (Clark et al. 2016), the frequency at which the opacity is unity is also uncertain.

Fig. 3 shows the median values of the parameters estimated from the optically thin model versus those estimated from the general-opacity models. As we discussed above, the estimates from the two types of model agree well for β, $\lambda_{\rm peak}$, and FIR luminosity, but there are systematic difference for $T_{\rm dust}$ and $M_{\rm dust}$. The probability distributions for the optically thin model are a good match to those for the subset of galaxies for which we know the size of the dust region, and therefore the parameter estimates we discuss in the rest of this paper have been derived using the optically thin model. The best-fitting optically thin SED parameters for all HerBS and SPT galaxies can be found in Appendices B1 and B2, respectively. The panels in Fig. 3 show the size of the systematic errors on these estimates if the dust is actually optically thick.

4.2 The β–dust temperature relationship

Where an MBB is fitted to an empirical SED it is well known that an artificial anticorrelation can be produced between dust temperature and β because of correlated errors in the two parameters (Shetty et al. 2009; Juvela & Ysard 2012; Kelly et al. 2012). Fig. 4 shows that there is a negative correlation between the measured values of β and dust temperature for both subsamples when assuming that the dust is optically thin. The strength of these correlations were tested with the Pearson correlation coefficient, $r_{\rm Pearson}$, and Spearman's rank correlation coefficient, $\rho_{\rm Spearman}$. The values ($r_{\rm Pearson} = -0.83$ and $\rho_{\rm Spearman} = -0.87$ for SPT; $r_{\rm Pearson} = -0.89$ and $\rho_{\rm Spearman} = -0.89$ for HerBS) show that the SPT and HerBS galaxies exhibit a strong negative β–$T_{\rm dust}$ correlation and the similarity between the two metrics suggests that few galaxies deviate from the trend. In the following section, we address the extent to which the observed β–$T_{\rm dust}$ anticorrelation is a true relationship between dust properties, reflecting an intrinsic change in the emissivity properties of dust grains with temperature, and how much is due to the fitting method.

4.3 Simulations

In order to assess how accurately our fitting routine derives a galaxy's dust parameters, we ran a suite of mock SEDs with known input parameters and measured how precisely we recover the dust properties from our fits. We generated these mock SEDs in the following way. We assumed that the dust emission is described by the optically thin model (equation 4). A catalogue of models were produced with dust parameters randomly drawn from a uniform distribution between the lower and upper bounds in Table 2, chosen to reflect the width of the posterior distributions for the parameters derived for the real sources. We created two samples of mock galaxies with similar properties to the real subsamples. To create the first sample, we placed each galaxy at a random redshift between 2 and 4 and gave the galaxy the same photometric coverage as for the HerBS subsample, omitting photometry at 1.2 mm as only a few of the HerBS sources have photometry at this wavelength. To create the second sample, we placed each galaxy at a random redshift between 2 and 6 and gave the galaxy the same photometric coverage as the SPT sample. We created observed SEDs of each mock galaxy by adding flux errors to the model SED, drawing randomly from a normal distribution with a standard deviation equal to the real observational error at that wavelength. We assumed a lensing magnification of 5.5× for all SPT galaxies and 5.3× for all HerBS galaxies, equal to the median lensing magnification for the two subsamples. Once we had calculated an observed SED for each mock galaxy, we removed it from the sample if it fell below the detection limits of the real samples (Section 2). For the sources that remained, we then derived the dust parameters using the same modelling procedure we had applied to the real sample.

Fig. 5 shows the parameters derived for the two artificial samples plotted against the input values of these parameters. There is good agreement between the input and output parameters. The rms error (RMSE) is calculated for each dust parameter, showing the intrinsic scatter around the 'true' input values. The RMSE indicate that our fitting recovers the input dust masses to 0.05 and 0.03 dex, the dust temperatures to 1.63 and 1.61 K and β to 0.13 and 0.09 of the input values for SPT and HerBS galaxies, respectively. The accuracy of the output $T_{\rm dust}$ decreases for higher temperatures as a result of the SED shifting to shorter wavelengths, meaning the peak is then less constrained by the *Herschel* photometry than at lower temperatures.

The right-most panel of the two simulations in Fig. 5 shows the difference between the input and output in the $T_{\rm dust}$–β plane. Since there is no intrinsic correlation between β and dust temperature in the model, the anticorrelation in this panel must have been introduced by correlated errors in the two parameters. The rms variations in β and $T_{\rm dust}$ in the artificial data set are 0.1 and 1.6 K, respectively. The rms variations in β and $T_{\rm dust}$ in the real data (Fig. 4) are 0.5 and 8 K, respectively, for the SPT galaxies, and 0.3 and 5 K, respectively, for the HerBS galaxies. The large differences between the rms values for the simulation and for the real samples imply there is a genuine inverse correlation between β and $T_{\rm dust}$ which is not caused by correlated measurement errors.

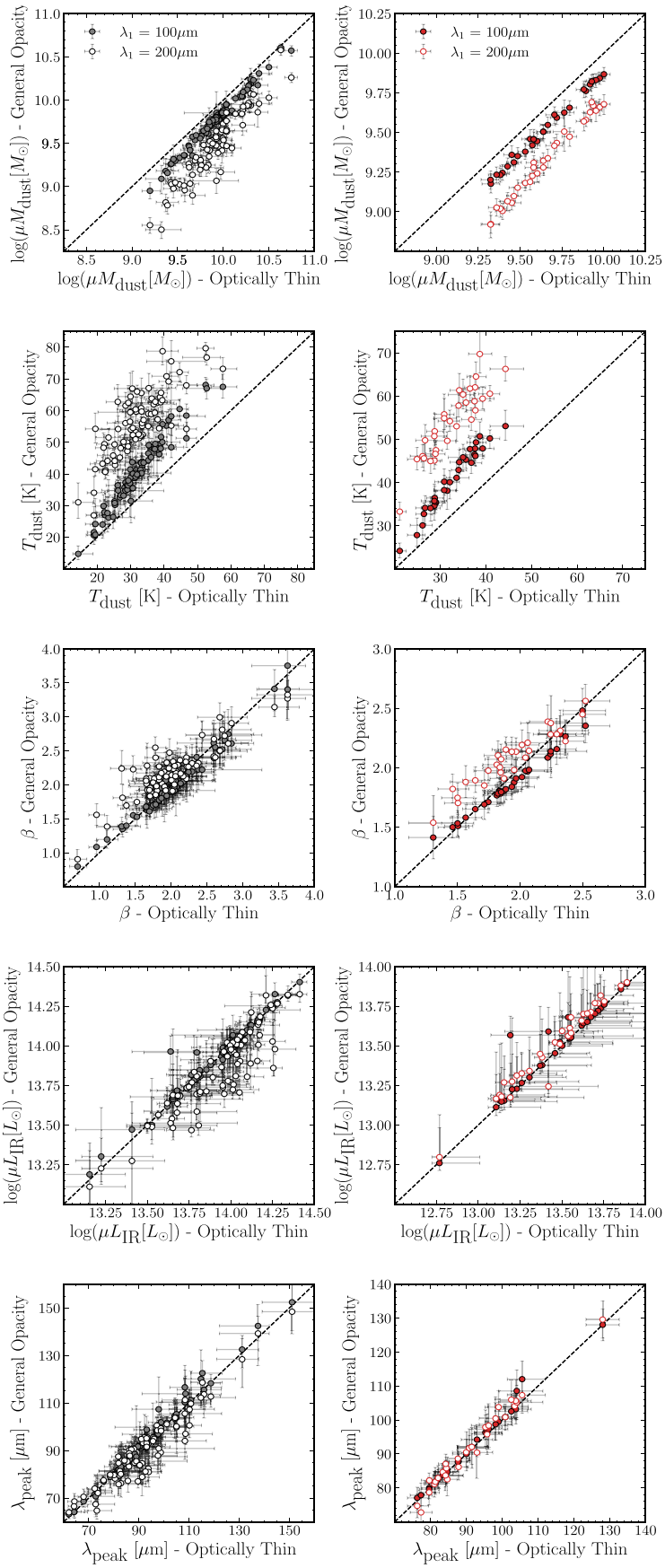

Figure 3. Comparison between the parameters derived from the optically thin and general-opacity models for the galaxies in the SPT (left column) and HerBS (right column) subsamples. The general opacity models are shown as filled and open circles for $\lambda_1 = 100$ μm and 200 μm, respectively.

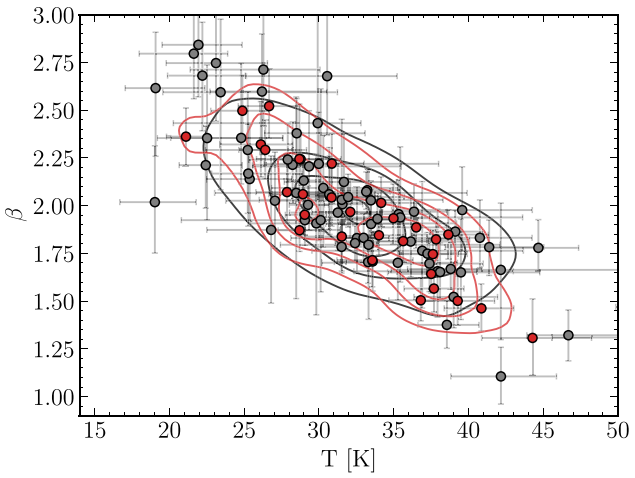

Figure 4. Relationship between the dust temperature and the emissivity index for the SPT (black) and HerBS (red) galaxies in the optically thin case.

Table 2. Upper and lower bounds assumed on the flat priors during the simulations described in Section 4.3.

Parameter	Bounds
$\log[\mu L_{\rm IR}(L_\odot)]$	13–14 (HerBS)
–	13–14.5 (SPT)
$T_{\rm dust}$ (K)	20–50
β	0.5–4
α	1–5

5 DISCUSSION

5.1 Evolution of β with redshift

Fig. 6 shows the distribution of galaxies in the β–z plane. The average value of the emissivity spectral index of SPT and HerBS galaxies ($\beta = 1.98$ and 1.91) are slightly higher than the values typically assumed for galaxies in the local Universe. It is significantly higher than the value in our Galaxy, which is remarkably uniform over the sky: $\beta = 1.51 \pm 0.01$ (Planck Collaboration XXII 2015). It is also significantly higher than the average value of β for a large sample of nearby galaxies (Lamperti et al. 2019), although it is close to the values measured for the most massive galaxies in this sample, which may be the descendants of the DSFGs (Eales et al. 2023). Considering the samples themselves, there is little evidence of any evolution in β over the redshift range $2 < z < 6$. The apparent negative redshift evolution within the HerBS sample is mostly the effect of the five sources at $z \sim 4$. At this redshift, the selection wavelength of HerBS, 500 μm, is close to the peak of the MBB, thus biasing us towards higher temperatures. The intrinsic anticorrelation between dust temperature and β (Section 4.2) would then explain the low values of β for these galaxies.

Similar conclusions have been reached in two other recent studies. For an independent sample of DSFGs selected from HerBS, Ismail et al. (2023) found no evolution in β over $2 < z < 3$. For a sample of 17 galaxies, Witstok et al. (2023) found no evolution across $4 < z < 8$.

5.2 Variation in β

To assess whether the variation of β in Fig. 6 is due to genuine differences in the properties of dust between DSFGs, or whether it is simply due to measurement errors, we repeated the simulations of the previous section. This time we used values of β drawn from a

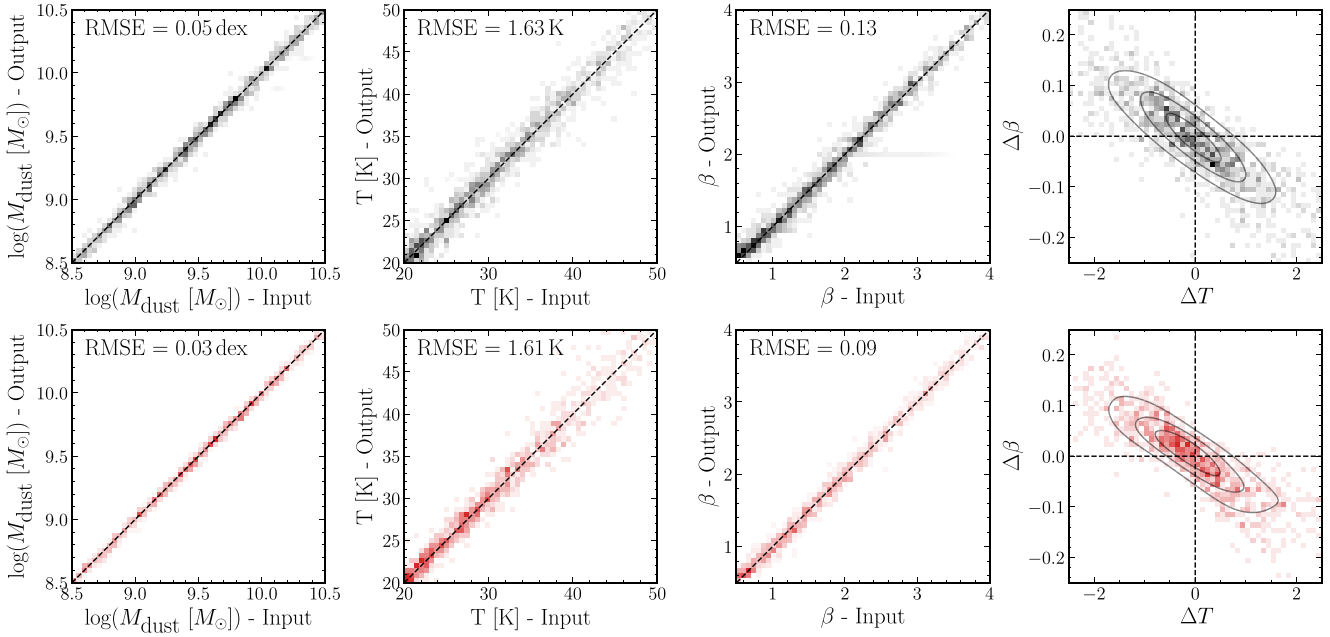

Figure 5. Comparison of the input and output (measured) values of dust mass, dust temperature, and dust emissivity index for the simulations described in Section 4.3. The right-most panel shows the difference between the input and output (measured) values of dust temperature against the difference between the input and output (measured) values of β. The top row (black) shows the results for the mock SPT galaxies and the bottom row (red) shows the results for the mock HerBS galaxies.

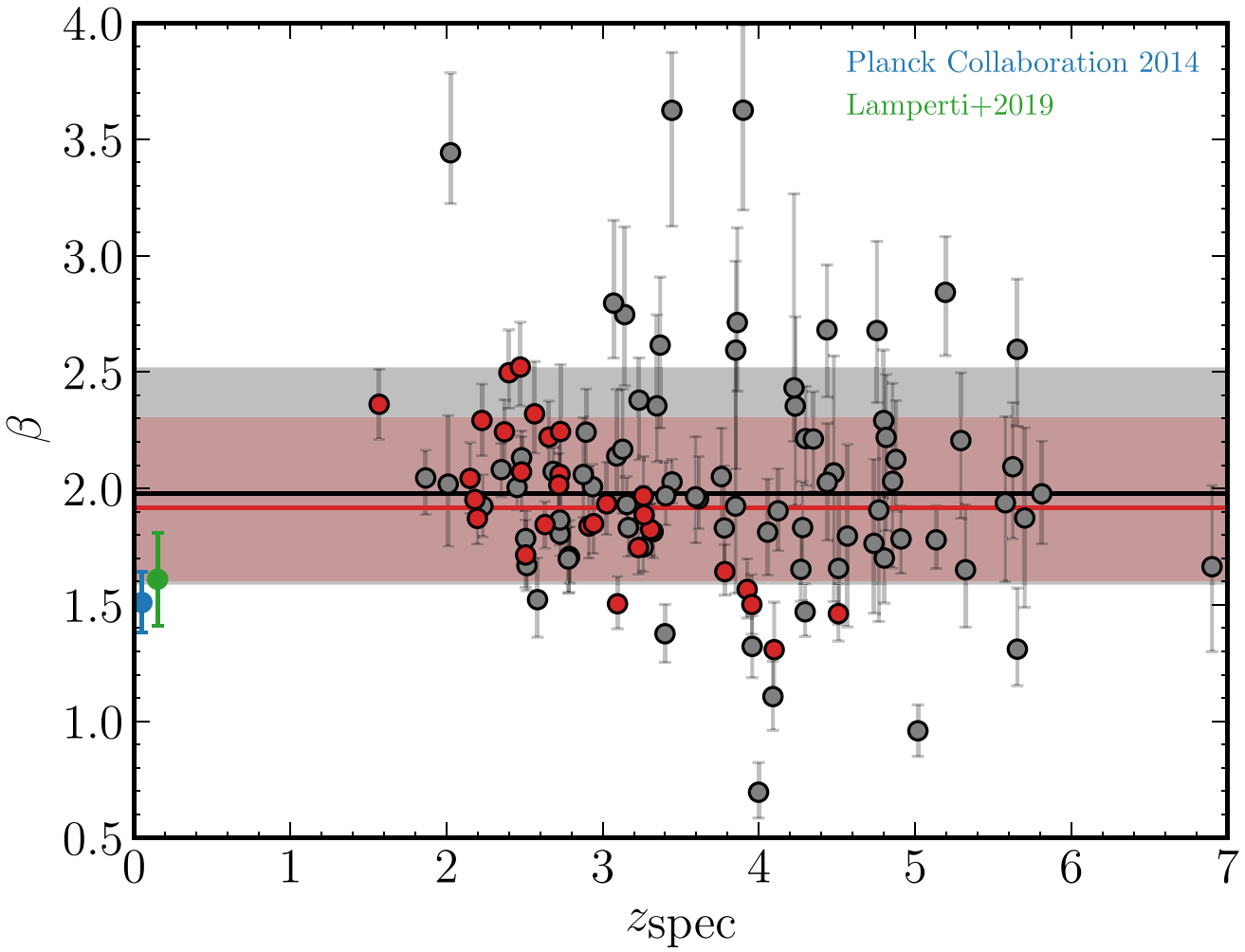

Figure 6. Distribution of β for the HerBS (red) and SPT (black) galaxies versus redshift, with the canonical values from JINGLES (green) and the Milky Way (blue). The median value of the stacked posterior distributions are shown as red and black lines for the HerBS and SPT subsamples, respectively, with the shaded regions showing the 16th to 84th percentiles.

uniform distribution covering the $\pm 1\sigma$ range of the observed values in Fig. 6, generating – as before – two samples of mock galaxies with observational data similar to that of the SPT and HerBS subsamples.

Fig. 7 shows a comparison of the input and output values of β as a function of redshift for both samples. There is no tendency for our fitting method to over- or underpredict the true value of β at any redshift. The rms scatter in Fig. 7 is $\simeq$0.1, which is much less than the rms scatter in β in Fig. 6 ($\simeq$0.3–0.5), which shows that the measurement errors are much smaller than the scatter in Fig. 6. Fig. 6 therefore shows that there are real differences in the properties of dust between DSFGs, a phenomenon also seen in the low-redshift galaxy population (Lamperti et al. 2019).

In their study of an independent sample of DSFGs drawn from HerBS, Ismail et al. (2023) reached similar conclusions. Across $2 < z < 4$, they found an average value of $\beta = 2.2 \pm 0.2$ with a range of β from 1.5 to 3.0, very similar to our results for the combined HerBS/SPT sample. They, too, concluded that the variation in β is caused by intrinsic differences between the dust in different DSFGs rather than by measurement errors. In their sample of 17 galaxies in the range $4 < z < 8$, Witstok et al. (2023) found a mean value of $\beta = 1.8 \pm 0.3$, in agreement with our estimates, with a similar wide range of β from $\simeq$1.5 to $\simeq$2.7. Other recent studies of high-redshift galaxies find similar values of β (da Cunha et al. 2021; Cooper et al. 2022).

Some of the SPT galaxies in Fig. 6 have values of $\beta \simeq 3$, as do galaxies in other high-redshift samples (Ismail et al. 2023; Witstok et al. 2023). Such values are higher than the global values seen in local galaxies (Lamperti et al. 2019), although such high values have been seen within Andromeda (Smith et al. 2012) and the Galaxy (Bracco et al. 2011). Are there any methodological limitations which might explain these results?

For our sample, one possible explanation might be the 3-mm photometry for the SPT sources. These flux densities were measured from ALMA images, so it is possible that they are too low because of the possibility – as with all interferometers – that some extended flux has been missed (the 'zero baseline problem'). We assessed how much would need to be lost by repeating the SED fitting without the 3-mm photometry, with $\beta = 2$. We did this for five sources: SPT0112−55 ($\beta = 3.62$), SPT0611−55 ($\beta = 3.44$), SPT2203−41 ($\beta = 2.84$), SPT2349−52 ($\beta = 3.62$), and SPT2357−51 ($\beta = 2.80$). Comparing the flux density at 3 mm predicted by the model with the observed flux density, we find that the observed flux density would need to be between 60 and 80 per cent lower than the true flux density to explain the very high values of β.

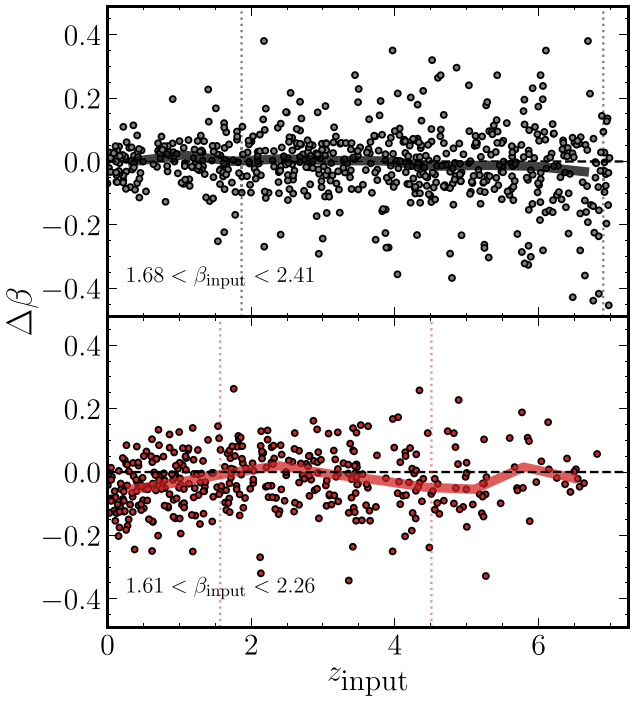

Figure 7. Difference between the input and output β values, $\Delta\beta = \beta_{\rm output} - \beta_{\rm input}$, as a function of the input redshift for mock SPT galaxies (top panel) and mock *Herschel* galaxies (bottom panel). Filled circles represent mock galaxies with SEDs that would have been observed according to their respective survey limits. Dotted vertical lines represent the minimum and maximum redshift observed in each subsample. The thick solid lines represent the median in $\Delta\beta$.

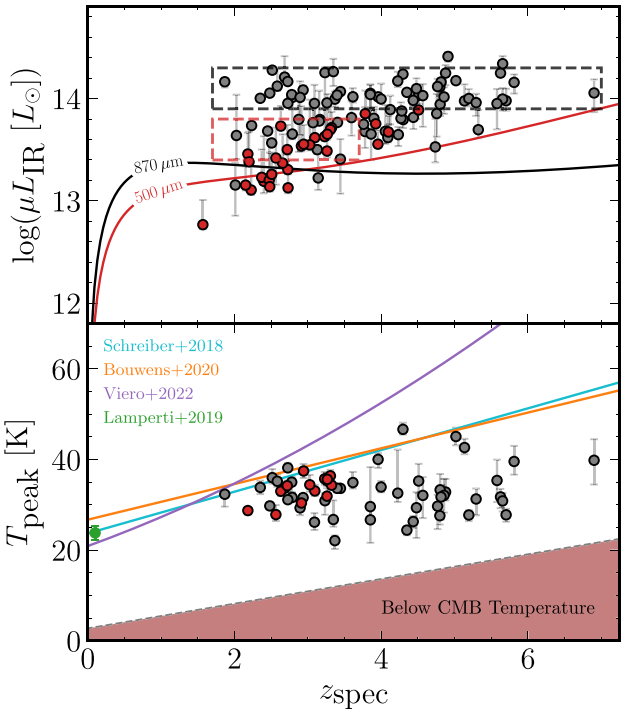

Figure 8. Top: distribution of HerBS (red) and SPT (black) galaxies in the $\mu L_{\rm IR}$–z plane. Red and black lines represent the detection limit of a source detected at > 80 mJy (500 μm) and > 25 mJy (870 μm) with $\beta = 2$ and $T_{\rm dust} = 32$ K. Boxed regions show the limits of the unbiased, luminosity-limited set of sources from which we test evolutionary trends in the dust temperature. Bottom: distribution of dust temperature with redshift for the sources selected in our luminosity-limited subset. Observed trends from Schreiber et al. (2018), Bouwens et al. (2020), and Viero et al. (2022) are illustrated as cyan, orange, and purple lines, respectively. The median dust temperature of local sources from JINGLES is shown in green.

Although this is possible, given the structures seen for high-redshift galaxies it seems unlikely, and it seems more likely to us that some of these extreme values found by us and others are genuine.

5.3 The inverse β–$T_{\rm dust}$ relationship

Our simulations imply that the inverse relationship seen between β and $T_{\rm dust}$ is not the result of measurement errors. Another study of an independent sample of HerBS sources reached a similar conclusion (Ismail et al. 2023). A similar conclusion was also reached by a hierarchical Bayesian study of nearby galaxies (Lamperti et al. 2019).

5.4 Evolution of $T_{\rm dust}$ with redshift

Does the temperature of dust increase with redshift? This has been a matter of intense debate in the literature. Some groups find evidence for an increase, e.g. Magdis et al. (2012), Magnelli et al. (2014), Swinbank et al. (2014), Béthermin et al. (2015), Ivison et al. (2016), Faisst et al. (2017), Schreiber et al. (2018), Zavala et al. (2018), Liang et al. (2019), Ma et al. (2019), Faisst et al. (2020), Bakx et al. (2021), and Witstok et al. (2023), which might not be surprising since both high specific star formation rates and lower dust abundances at high redshift might lead to higher dust temperatures. Others report a fall, e.g. Symeonidis et al. (2013). An important caveat, noted by many of those studies, is the correlation between dust temperature and luminosity (Dunne et al. 2000) which – since galaxies at high redshift tend to have high luminosities – might lead to a correlation between dust temperature and redshift. In contrast, the works of Casey et al. (2018), Jin et al. (2019), Dudzevičiūtė et al. (2020), Lim et al. (2020), Reuter et al. (2020), Barger et al. (2022), Drew & Casey (2022), and Witstok et al. (2023), among others, report little or no evolution of temperature with redshift at a given fixed IR luminosity.

The dust temperature derived from SED fitting depends on the model assumed for the dust opacity, whereas $\lambda_{\rm peak}$ is the same for every model. To avoid this dependence, we have derived $\lambda_{\rm peak}$ for each source and then calculated $T_{\rm dust}$ from Wien's displacement law. Although this will not be the same as the true temperature of the dust, it allows us to see whether there is any evidence for a change in $T_{\rm dust}$ with redshift.

The top panel of Fig. 8 shows the distribution of IR luminosity for the full sample of galaxies as obtained from the fitting of equation (4), as well as the detection limits. In calculating the detection limits, we have assumed an SED with a dust temperature of 32 K, the median temperature of the sample, and $\beta = 2$. To avoid the selection effect caused by the luminosity–temperature relationship, we only consider sources selected in a small range of IR luminosity, as illustrated by the boxed regions. The bottom panel of Fig. 8 shows the peak dust temperature [$T_{\rm peak} = 2.898 \times 10^3$ (μmK)/$\lambda_{\rm peak}$ (μm)] versus redshift. We have plotted the observational relationships inferred by Schreiber et al. (2018), Bouwens et al. (2020), and Viero et al. (2022). Bootstrap fitting with a linear model gives an evolution rate of 5.20 ± 0.92 and -0.25 ± 0.52 $T_{\rm peak}/z$ for the HerBS and SPT galaxies, respectively. In a study of an independent sample of HerBS galaxies, Ismail et al. (2023) found a rate of evolution of 6.5 ± 0.5 K/z, similar to our value.

While there is statistical evidence within the HerBS subsample – both ours and that of Ismail et al. (2023) – for the evolution of

temperature with redshift, there seems little evidence for any such evolution over the redshift range covered by the combined HerBS and SPT sample.

We suggest there is a simple selection effect that explains the temperature evolution seen in the HerBS sample. For the highest redshift sources in the HerBS subsample, the selection wavelength in the rest frame is close to the peak of the MBB, which leads to a selection bias towards sources with higher temperatures. Given the lack of any obvious correlation when both subsamples are considered together, we conclude that there is no strong evidence for temperature evolution. A plausible suggestion for the disagreement in the literature was suggested by Drew & Casey (2022): the studies that have found no evolution are those that looked for evolution at a fixed infrared luminosity, as in this paper, whereas those that found evolution were generally looking for evolution at a fixed stellar mass. The latter would be expected to see evolution because of the gradual increase in specific star formation rate – and thus the increase in the intensity of the interstellar radiation field – with redshift.

6 CONCLUSIONS

In this paper, we estimate values of β and dust temperature for a sample of 109 DSFGs spanning $2 < z < 6$. We have obtained the following results:

(i) We have compared the results from fitting the emission from the galaxies with an optically thin model and with two general-opacity models, one in which the dust becomes optically thick at a wavelength of 100 μm, the other where the dust becomes optically thick at 200 μm. We find that our estimates of β, the peak of the galaxy SED, and the FIR luminosity, are similar between the models, although there is a change in β of 0.2 between the most extreme models. In contrast, our estimates of dust mass and dust temperature depend strongly on the opacity assumptions.

(ii) For a subsample of 37 galaxies, we have measurements of the sizes of the sources, which allows us to estimate the opacity directly. We find very similar estimates of the galaxy parameters with this model to the optically thin model, which we use for the rest of the paper.

(iii) We find no evidence of any change in β with redshift across $2 < z < 6$, with a median value of $\beta = 1.96$ for the optically thin model and a 14–86 per cent confidence interval for the population of 1.65–2.38. Using simulations, we estimate the measurement errors from our procedure and show that the variation of β in the population is the result of intrinsic variations in the properties of the dust in DSFGs, the same found between galaxies in the low-redshift Universe (Lamperti et al. 2019).

(iv) After allowing for the effect of correlated errors, we find an inverse correlation between our estimates of β and dust temperature.

(v) We find no evidence at a fixed FIR luminosity for any change in dust temperature with redshift.

The results in this and other recent papers show that the properties of dust appear to differ between galaxies, both at high and low redshift. Ours and other recent papers show that there appears to be intrinsic anticorrelation between dust emissivity index and dust temperature. As far as we know, there is no chemical/physical model of dust that explains either of these results.

ACKNOWLEDGEMENTS

BW thanks the Engineering and Physical Sciences Research Council for a PhD studentship. SAE thanks the Science and Technology Facilities Council (consolidated grant ST/K000926/1) for the funds that supported this research.

DATA AVAILABILITY

The photometry for each galaxy and the results of fitting our models to the photometry are listed in the appendix.

REFERENCES

Bakx T. J. L. C. et al., 2018, MNRAS, 473, 1751
Bakx T. J. L. C. et al., 2021, MNRAS, 508, L58
Barger A. J., Cowie L. L., Sanders D. B., Fulton E., Taniguchi Y., Sato Y., Kawara K., Okuda H., 1998, Nature, 394, 248
Barger A. J., Cowie L. L., Blair A. H., Jones L. H., 2022, ApJ, 934, 56
Bendo G. J. et al., 2023, MNRAS, 522, 2995
Béthermin M. et al., 2015, A&A, 573, A113
Blain A. W., Longair M. S., 1993, MNRAS, 264, 509
Blain A. W., Smail I., Ivison R. J., Kneib J. P., Frayer D. T., 2002, Phys. Rep., 369, 111
Bouwens R. et al., 2020, ApJ, 902, 112
Bracco A. et al., 2011, MNRAS, 412, 1151
Casey C. M., Narayanan D., Cooray A., 2014, Phys. Rep., 541, 45
Casey C. M. et al., 2018, ApJ, 862, 77
Casey C. M. et al., 2019, ApJ, 887, 55
Casey C. M. et al., 2021, ApJ, 923, 215
Clark C. J. R., Schofield S. P., Gomez H. L., Davies J. I., 2016, MNRAS, 459, 1646
Clark C. J. R., Roman-Duval J. C., Gordon K. D., Bot C., Smith M. W. L., Hagen L. M. Z., 2023, ApJ, 946, 42
Conley A. et al., 2011, ApJ, 732, L35
Cooper O. R., Casey C. M., Zavala J. A., Champagne J. B., da Cunha E., Long A. S., Spilker J. S., Staguhn J., 2022, ApJ, 930, 32
Cortzen I. et al., 2020, A&A, 634, L14
da Cunha E. et al., 2013, ApJ, 766, 13
da Cunha E. et al., 2015, ApJ, 806, 110
da Cunha E. et al., 2021, ApJ, 919, 30
Dole H. et al., 2006, A&A, 451, 417
Draine B. T., Lee H. M., 1984, ApJ, 285, 89
Draine B. T. et al., 2014, ApJ, 780, 172
Drew P. M., Casey C. M., 2022, ApJ, 930, 142
Driver S. P., Popescu C. C., Tuffs R. J., Graham A. W., Liske J., Baldry I., 2008, ApJ, 678, L101
Dudzevičiūtė U. et al., 2020, MNRAS, 494, 3828
Dunne L., Eales S., Edmunds M., Ivison R., Alexander P., Clements D. L., 2000, MNRAS, 315, 115
Dunne L., Maddox S. J., Papadopoulos P. P., Ivison R. J., Gomez H. L., 2022, MNRAS, 517, 962
Dwek E. et al., 1998, ApJ, 508, 106
Eales S., Lilly S., Gear W., Dunne L., Bond J. R., Hammer F., Le Fèvre O., Crampton D., 1999, ApJ, 515, 518
Eales S. et al., 2010, PASP, 122, 499
Eales S. et al., 2012, ApJ, 761, 168
Eales S., Gomez H., Dunne L., Dye S., Smith M. W. L., 2023, preprint (arXiv:2303.07376)
Everett W. B. et al., 2020, ApJ, 900, 55
Faisst A. L. et al., 2017, ApJ, 847, 21
Faisst A. L., Fudamoto Y., Oesch P. A., Scoville N., Riechers D. A., Pavesi R., Capak P., 2020, MNRAS, 498, 4192
Fixsen D. J., Dwek E., Mather J. C., Bennett C. L., Shafer R. A., 1998, ApJ, 508, 123
Galliano F., Galametz M., Jones A. P., 2018, ARA&A, 56, 673
Hagimoto M. et al., 2023, MNRAS, 521, 5508
Harris A. I. et al., 2012, ApJ, 752, 152
Holland W. S. et al., 1999, MNRAS, 303, 659
Holland W. S. et al., 2013, MNRAS, 430, 2513
Hughes D. H. et al., 1998, Nature, 394, 241

Hunt L. K. et al., 2015, A&A, 576, A33
Ikarashi S. et al., 2017, ApJ, 849, L36
Ismail D. et al., 2023, A&A 678 A27
Ivison R. J. et al., 2016, ApJ, 832, 78
James A., Dunne L., Eales S., Edmunds M. G., 2002, MNRAS, 335, 753
Jin S. et al., 2019, ApJ, 887, 144
Juvela M., Ysard N., 2012, A&A, 541, A33
Kelly B. C., Shetty R., Stutz A. M., Kauffmann J., Goodman A. A., Launhardt R., 2012, ApJ, 752, 55
Lamperti I. et al., 2019, MNRAS, 489, 4389
Li Q., Narayanan D., Davé R., 2019, MNRAS, 490, 1425
Liang L. et al., 2019, MNRAS, 489, 1397
Lilly S. J., Le Fevre O., Hammer F., Crampton D., 1996, ApJ, 460, L1
Lim C.-F. et al., 2020, ApJ, 889, 80
Ma X. et al., 2019, MNRAS, 487, 1844
Magdis G. E. et al., 2012, ApJ, 760, 6
Magnelli B. et al., 2014, A&A, 561, A86
McKay S. J., Barger A. J., Cowie L. L., Bauer F. E., Rosenthal M. J. N., 2023, ApJ, 951, 48
Millard J. S. et al., 2020, MNRAS, 494, 293
Montaña A. et al., 2021, MNRAS, 505, 5260
Oliver S. J. et al., 2012, MNRAS, 424, 1614
Planck Collaboration XXII, 2015, A&A, 576, A107
Planck Collaboration VI, 2020, A&A, 641, A6
Popping G., Péroux C., 2022, MNRAS, 513, 1531
Popping G., Somerville R. S., Galametz M., 2017, MNRAS, 471, 3152
Puget J. L., Abergel A., Bernard J. P., Boulanger F., Burton W. B., Desert F. X., Hartmann D., 1996, A&A, 308, L5
Reuter C. et al., 2020, ApJ, 902, 78
Schreiber C., Elbaz D., Pannella M., Ciesla L., Wang T., Franco M., 2018, A&A, 609, A30
Scoville N. et al., 2014, ApJ, 783, 84
Scoville N. et al., 2016, ApJ, 820, 83
Scoville N. et al., 2017, ApJ, 837, 150
Shapley A. E., Cullen F., Dunlop J. S., McLure R. J., Kriek M., Reddy N. A., Sanders R. L., 2020, ApJ, 903, L16
Shetty R., Kauffmann J., Schnee S., Goodman A. A., 2009, ApJ, 696, 676
Smail I., Ivison R. J., Blain A. W., 1997, ApJ, 490, L5
Smith M. W. L. et al., 2012, ApJ, 756, 40
Spilker J. S. et al., 2016, ApJ, 826, 112
Strandet M. L. et al., 2016, ApJ, 822, 80
Swinbank A. M. et al., 2014, MNRAS, 438, 1267
Symeonidis M. et al., 2013, MNRAS, 431, 2317
Tabatabaei F. S. et al., 2014, A&A, 561, A95
Tacconi L. J. et al., 2010, Nature, 463, 781
Urquhart S. A. et al., 2022, MNRAS, 511, 3017
Vieira J. D. et al., 2010, ApJ, 719, 763
Viero M. P., Sun G., Chung D. T., Moncelsi L., Condon S. S., 2022, MNRAS, 516, L30
Wang W.-H. et al., 2017, ApJ, 850, 37
Weiß A. et al., 2013, ApJ, 767, 88
Whitworth A. P. et al., 2019, MNRAS, 489, 5436
Witstok J., Jones G. C., Maiolino R., Smit R., Schneider R., 2023, MNRAS, 523, 3119
Zavala J. A. et al., 2018, MNRAS, 475, 5585
Zhang Z.-Y., Papadopoulos P. P., Ivison R. J., Galametz M., Smith M. W. L., Xilouris E. M., 2016, R. Soc. Open Sci., 3, 160025

APPENDIX A: HERBS PHOTOMETRY

Table A1. Spectroscopic redshifts, lensing magnifications, and photometry for HerBS sources.

Source	Spec-z	μ	$S_{250\,\mu m}$ (mJy)	$S_{350\,\mu m}$ (mJy)	$S_{500\,\mu m}$ (mJy)	$S_{850\,\mu m}$ (mJy)	$S_{1.2\,mm}$ (mJy)	$S_{2\,mm}$ (mJy)	$S_{3\,mm}$ (mJy)
HerBS-11	2.631	18.4	257.5 ± 6.4	271.1 ± 6.3	204.0 ± 7.2	67.3 ± 6.3	–	3.59 ± 0.03	0.93 ± 0.02
HerBS-14	3.782	36.4	116.3 ± 6.1	177.0 ± 6.3	179.3 ± 7.5	77.9 ± 6.4	28.9 ± 0.6	7.31 ± 0.04	1.50 ± 0.02
HerBS-18	2.182	27.9	212.9 ± 4.7	244.2 ± 5.0	169.4 ± 6.2	52.9 ± 6.1	–	2.73 ± 0.03	0.74 ± 0.06
HerBS-21	3.323	6.1	125.8 ± 5.5	185.5 ± 5.8	155.1 ± 7.4	51.3 ± 6.3	–	3.92 ± 0.03	0.94 ± 0.10
HerBS-24	2.198	4.6	170.9 ± 5.7	197.1 ± 6.3	145.6 ± 7.4	64.8 ± 7.8	–	2.68 ± 0.03	0.74 ± 0.03
HerBS-25	2.912	49.8	112.5 ± 5.0	148.0 ± 5.4	143.4 ± 6.5	49.2 ± 5.7	–	3.52 ± 0.03	0.81 ± 0.11
HerBS-27	4.509	14.6	72.2 ± 5.3	129.8 ± 5.6	138.6 ± 7.0	90.5 ± 6.3	28.9 ± 1.0	8.70 ± 0.03	1.97 ± 0.02
HerBS-28	3.925	5.7	79.4 ± 5.8	135.4 ± 6.0	140.0 ± 7.4	79.4 ± 7.8	25.5 ± 1.2	5.56 ± 0.03	1.66 ± 0.10
HerBS-36	3.095	5.4	121.5 ± 6.1	161.0 ± 6.7	125.5 ± 7.7	64.0 ± 8.8	–	4.81 ± 0.03	1.11 ± 0.02
HerBS-39	3.229	5.1	118.3 ± 5.1	141.2 ± 5.5	119.7 ± 6.8	36.5 ± 7.0	–	3.01 ± 0.03	0.64 ± 0.03
HerBS-41	4.098	2.1	63.3 ± 6.2	91.1 ± 6.1	121.7 ± 7.4	31.8 ± 5.9	15.2 ± 0.5	4.85 ± 0.07	–
HerBS-42	3.307	3.9	130.3 ± 5.8	160.0 ± 6.1	116.2 ± 6.8	50.4 ± 6.1	–	2.95 ± 0.06	0.58 ± 0.05
HerBS-49	2.727	15.3	76.8 ± 6.0	110.9 ± 6.2	110.4 ± 7.3	31.9 ± 8.5	–	1.69 ± 0.04	1.13 ± 0.09
HerBS-55	2.656	13.7	109.0 ± 5.3	116.5 ± 5.5	107.1 ± 6.6	29.9 ± 7.1	–	1.05 ± 0.03	0.33 ± 0.02
HerBS-57	3.265	15.0	118.1 ± 4.9	147.3 ± 5.2	105.4 ± 6.4	60.7 ± 8.5	–	3.05 ± 0.02	0.50 ± 0.02
HerBS-60	3.261	9.5	73.3 ± 5.8	101.2 ± 6.1	103.6 ± 7.5	39.8 ± 5.7	13.2 ± 0.8	2.54 ± 0.03	0.53 ± 0.02
HerBS-68	2.719	10.5	139.1 ± 5.3	144.8 ± 5.4	100.5 ± 6.6	46.7 ± 7.7	–	1.62 ± 0.04	0.32 ± 0.05
HerBS-73	3.026	3.1	117.1 ± 6.0	129.0 ± 6.2	99.6 ± 7.4	49.4 ± 6.8	–	2.09 ± 0.03	0.43 ± 0.02
HerBS-86	2.564	4.8	77.4 ± 5.6	90.7 ± 5.8	96.0 ± 7.4	33.8 ± 6.1	8.1 ± 0.6	1.56 ± 0.02	0.25 ± 0.02
HerBS-93	2.400	2.4	77.3 ± 5.4	87.3 ± 5.7	94.8 ± 7.0	22.8 ± 5.7	6.2 ± 0.4	1.39 ± 0.02	0.16 ± 0.01
HerBS-103	2.942	4.3	126.1 ± 5.3	131.2 ± 5.7	93.5 ± 7.0	33.7 ± 7.6	–	1.40 ± 0.03	0.42 ± 0.02
HerBS-111	2.371	4.3	105.9 ± 6.5	115.6 ± 6.2	92.7 ± 7.4	13.3 ± 6.9	–	1.13 ± 0.02	0.21 ± 0.02
HerBS-132	2.473	4.8	86.7 ± 5.8	102.6 ± 6.0	90.6 ± 7.8	16.6 ± 7.4	–	0.86 ± 0.02	0.16 ± 0.02
HerBS-145	2.730	1.9	54.7 ± 6.0	67.4 ± 6.2	86.8 ± 7.7	13.4 ± 7.0	5.1 ± 0.6	1.06 ± 0.04	–
HerBS-160	3.955	8.1	48.6 ± 5.6	84.2 ± 6.0	84.8 ± 7.1	36.6 ± 6.4	15.0 ± 0.6	3.94 ± 0.02	0.91 ± 0.02
HerBS-182	2.227	1.1	89.0 ± 5.7	109.1 ± 6.2	82.3 ± 7.9	–	–	1.04 ± 0.03	0.21 ± 0.02
HerBS-184	2.507	6.0	91.9 ± 5.9	107.6 ± 6.0	82.3 ± 7.1	–	–	1.49 ± 0.02	0.48 ± 0.02
HerBS-200	2.151	0.4	107.1 ± 6.1	109.7 ± 6.0	80.5 ± 7.5	11.3 ± 6.6	–	0.78 ± 0.02	0.25 ± 0.01
HerBS-207	1.569	5.2	96.9 ± 5.9	121.7 ± 6.1	80.2 ± 7.5	33.1 ± 6.3	–	0.89 ± 0.02	0.25 ± 0.03
HerBS-208	2.481	1.4	69.4 ± 5.1	91.9 ± 5.5	80.1 ± 6.6	–	–	1.40 ± 0.05	0.32 ± 0.04

APPENDIX B: BEST-FITTING SED PARAMETER

Table B1. Best-fitting SED parameters for all HerBS sources.

Source	Spec-z	$\log[M_{\rm dust}\ (\mathrm{M}_\odot)]$	$T_{\rm dust}$ (K)	β	χ^2_ν
HerBS-11	2.631	$8.63^{+0.03}_{-0.04}$	$34.01^{+1.78}_{-1.58}$	$1.84^{+0.10}_{-0.10}$	1.63
HerBS-14	3.782	$8.42^{+0.04}_{-0.03}$	$37.51^{+1.77}_{-2.08}$	$1.64^{+0.12}_{-0.10}$	1.45
HerBS-18	2.182	$8.47^{+0.03}_{-0.04}$	$29.05^{+1.45}_{-1.29}$	$1.95^{+0.11}_{-0.11}$	0.94
HerBS-21	3.323	$9.01^{+0.04}_{-0.04}$	$35.63^{+1.73}_{-1.70}$	$1.81^{+0.12}_{-0.11}$	0.18
HerBS-24	2.198	$9.27^{+0.04}_{-0.04}$	$28.70^{+1.65}_{-1.43}$	$1.87^{+0.11}_{-0.11}$	3.60
HerBS-25	2.912	$8.18^{+0.05}_{-0.05}$	$31.53^{+1.91}_{-2.51}$	$1.84^{+0.17}_{-0.14}$	1.56
HerBS-27	4.509	$8.84^{+0.04}_{-0.04}$	$40.87^{+2.16}_{-2.49}$	$1.46^{+0.13}_{-0.12}$	3.56
HerBS-28	3.925	$9.20^{+0.04}_{-0.04}$	$37.69^{+2.01}_{-1.99}$	$1.57^{+0.13}_{-0.12}$	1.70
HerBS-36	3.095	$9.20^{+0.04}_{-0.04}$	$36.81^{+2.29}_{-2.13}$	$1.50^{+0.12}_{-0.11}$	1.80
HerBS-39	3.229	$8.93^{+0.04}_{-0.04}$	$37.62^{+2.30}_{-2.29}$	$1.75^{+0.13}_{-0.12}$	1.06
HerBS-41	4.098	$9.44^{+0.06}_{-0.07}$	$44.29^{+3.95}_{-3.40}$	$1.31^{+0.20}_{-0.20}$	8.36
HerBS-42	3.307	$9.01^{+0.04}_{-0.04}$	$37.83^{+2.24}_{-2.00}$	$1.82^{+0.11}_{-0.11}$	1.99
HerBS-49	2.727	$8.48^{+0.05}_{-0.05}$	$28.93^{+2.14}_{-2.08}$	$2.06^{+0.19}_{-0.18}$	14.77
HerBS-55	2.656	$8.26^{+0.04}_{-0.04}$	$30.86^{+2.17}_{-2.09}$	$2.22^{+0.16}_{-0.15}$	7.48
HerBS-57	3.265	$8.40^{+0.05}_{-0.04}$	$36.51^{+2.04}_{-2.33}$	$1.89^{+0.13}_{-0.11}$	6.40
HerBS-60	3.261	$8.66^{+0.04}_{-0.04}$	$32.10^{+2.16}_{-2.58}$	$1.97^{+0.17}_{-0.14}$	1.09
HerBS-68	2.719	$8.44^{+0.04}_{-0.04}$	$34.16^{+2.22}_{-1.99}$	$2.01^{+0.14}_{-0.13}$	2.97
HerBS-73	3.026	$9.04^{+0.05}_{-0.04}$	$34.99^{+2.41}_{-3.22}$	$1.93^{+0.18}_{-0.13}$	3.95
HerBS-86	2.564	$8.88^{+0.06}_{-0.05}$	$26.11^{+2.13}_{-2.72}$	$2.32^{+0.22}_{-0.17}$	3.73
HerBS-93	2.400	$9.07^{+0.06}_{-0.05}$	$24.88^{+1.79}_{-2.12}$	$2.50^{+0.18}_{-0.15}$	6.77
HerBS-103	2.942	$8.75^{+0.04}_{-0.04}$	$38.66^{+2.67}_{-2.46}$	$1.85^{+0.13}_{-0.13}$	2.53
HerBS-111	2.371	$8.79^{+0.05}_{-0.05}$	$28.77^{+1.92}_{-1.75}$	$2.24^{+0.14}_{-0.14}$	2.00
HerBS-132	2.473	$8.64^{+0.05}_{-0.05}$	$26.67^{+2.04}_{-2.06}$	$2.52^{+0.19}_{-0.17}$	1.69
HerBS-145	2.730	$9.04^{+0.05}_{-0.06}$	$28.69^{+2.79}_{-2.87}$	$2.24^{+0.29}_{-0.24}$	7.24
HerBS-160	3.955	$8.81^{+0.04}_{-0.04}$	$39.28^{+2.46}_{-2.36}$	$1.50^{+0.13}_{-0.13}$	0.52
HerBS-182	2.227	$9.44^{+0.05}_{-0.05}$	$26.41^{+1.84}_{-1.77}$	$2.29^{+0.16}_{-0.15}$	0.39
HerBS-184	2.507	$8.80^{+0.04}_{-0.05}$	$33.57^{+2.73}_{-2.37}$	$1.71^{+0.15}_{-0.14}$	4.62
HerBS-200	2.151	$9.76^{+0.05}_{-0.05}$	$30.84^{+2.68}_{-2.21}$	$2.04^{+0.15}_{-0.15}$	5.58
HerBS-207	1.569	$8.99^{+0.05}_{-0.05}$	$21.10^{+1.39}_{-1.30}$	$2.36^{+0.15}_{-0.15}$	3.43
HerBS-208	2.481	$9.45^{+0.06}_{-0.05}$	$27.87^{+2.11}_{-2.08}$	$2.07^{+0.18}_{-0.16}$	0.96

Table B2. Best-fitting SED parameters for all SPT sources.

Source	Spec-z	$\log[M_{\rm dust}\ (\mathrm{M}_\odot)]$	$T_{\rm dust}$ [K]	β	χ^2_ν
SPT0002-52	2.351	$8.95^{+0.05}_{-0.05}$	$33.23^{+2.19}_{-1.80}$	$2.08^{+0.11}_{-0.12}$	2.05
SPT0020-51	4.123	$9.16^{+0.06}_{-0.06}$	$33.49^{+3.02}_{-3.04}$	$1.90^{+0.18}_{-0.17}$	0.57
SPT0027-50	3.444	$9.29^{+0.04}_{-0.04}$	$33.48^{+1.35}_{-1.25}$	$2.03^{+0.10}_{-0.09}$	3.02
SPT0054-41	4.877	$9.26^{+0.08}_{-0.06}$	$31.67^{+3.54}_{-3.99}$	$2.12^{+0.25}_{-0.22}$	0.84
SPT0103-45	3.090	$9.57^{+0.08}_{-0.07}$	$25.37^{+2.84}_{-2.88}$	$2.14^{+0.29}_{-0.22}$	1.10
SPT0106-64	4.910	$9.21^{+0.05}_{-0.05}$	$41.39^{+3.65}_{-2.93}$	$1.78^{+0.14}_{-0.15}$	3.65
SPT0109-47	3.614	$8.78^{+0.05}_{-0.05}$	$35.33^{+2.12}_{-3.32}$	$1.96^{+0.18}_{-0.13}$	2.85
SPT0112-55	3.443	$9.18^{+0.24}_{-0.35}$	$14.35^{+4.40}_{-1.59}$	$3.62^{+0.25}_{-0.50}$	6.53
SPT0113-46	4.233	$8.84^{+0.13}_{-0.12}$	$22.52^{+5.08}_{-3.33}$	$2.35^{+0.38}_{-0.43}$	1.40
SPT0125-47	2.515	$9.47^{+0.05}_{-0.05}$	$38.81^{+2.07}_{-2.88}$	$1.67^{+0.14}_{-0.11}$	2.69
SPT0125-50	3.957	$8.77^{+0.06}_{-0.06}$	$46.69^{+3.35}_{-2.78}$	$1.32^{+0.13}_{-0.13}$	3.83
SPT0136-63	4.299	$9.18^{+0.07}_{-0.06}$	$28.24^{+2.68}_{-2.68}$	$2.21^{+0.22}_{-0.20}$	0.42
SPT0147-64	4.803	$9.30^{+0.07}_{-0.06}$	$35.28^{+3.98}_{-5.08}$	$1.70^{+0.27}_{-0.19}$	2.39
SPT0150-59	2.788	$9.26^{+0.05}_{-0.05}$	$33.29^{+1.88}_{-2.26}$	$1.70^{+0.13}_{-0.11}$	2.63
SPT0155-62	4.349	$10.01^{+0.07}_{-0.07}$	$22.43^{+2.40}_{-1.78}$	$2.21^{+0.20}_{-0.23}$	3.32
SPT0202-61	5.018	$9.12^{+0.04}_{-0.04}$	$57.61^{+4.19}_{-3.64}$	$0.96^{+0.11}_{-0.11}$	6.46
SPT0226-45	3.233	$9.01^{+0.07}_{-0.08}$	$28.51^{+4.58}_{-2.15}$	$2.38^{+0.18}_{-0.26}$	4.29
SPT0243-49	5.702	$9.67^{+0.11}_{-0.09}$	$26.80^{+4.61}_{-4.30}$	$1.87^{+0.39}_{-0.38}$	0.71
SPT0245-63	5.626	$9.84^{+0.08}_{-0.08}$	$30.30^{+4.99}_{-3.47}$	$2.09^{+0.28}_{-0.31}$	1.07
SPT0300-46	3.595	$9.35^{+0.07}_{-0.07}$	$31.26^{+2.94}_{-3.23}$	$1.96^{+0.26}_{-0.20}$	0.96
SPT0311-58	6.901	$9.28^{+0.09}_{-0.08}$	$42.17^{+10.20}_{-7.33}$	$1.66^{+0.35}_{-0.37}$	1.37
SPT0314-44	2.935	$9.44^{+0.04}_{-0.04}$	$31.57^{+1.35}_{-1.22}$	$2.01^{+0.10}_{-0.09}$	2.96
SPT0319-47	4.510	$9.38^{+0.09}_{-0.08}$	$37.93^{+5.07}_{-5.60}$	$1.66^{+0.33}_{-0.24}$	1.63
SPT0345-47	4.296	$8.85^{+0.06}_{-0.06}$	$52.45^{+2.45}_{-2.60}$	$1.47^{+0.12}_{-0.11}$	1.22
SPT0346-52	5.655	$9.24^{+0.05}_{-0.06}$	$52.76^{+4.10}_{-7.17}$	$1.31^{+0.26}_{-0.16}$	2.94
SPT0348-62	5.654	$9.59^{+0.14}_{-0.12}$	$26.19^{+4.35}_{-3.48}$	$2.60^{+0.30}_{-0.33}$	0.21
SPT0402-45	2.683	$9.46^{+0.04}_{-0.04}$	$33.16^{+1.60}_{-1.62}$	$2.07^{+0.10}_{-0.09}$	8.22
SPT0403-58	4.056	$9.40^{+0.07}_{-0.07}$	$36.14^{+3.77}_{-4.35}$	$1.81^{+0.23}_{-0.19}$	2.28
SPT0418-47	4.225	$8.30^{+0.19}_{-0.09}$	$29.92^{+2.89}_{-9.65}$	$2.43^{+0.83}_{-0.23}$	7.44
SPT0425-40	5.135	$8.78^{+0.05}_{-0.05}$	$44.68^{+2.69}_{-3.05}$	$1.78^{+0.15}_{-0.12}$	4.65
SPT0436-40	3.852	$9.20^{+0.16}_{-0.16}$	$23.42^{+7.81}_{-3.87}$	$2.59^{+0.38}_{-0.51}$	2.63
SPT0441-46	4.480	$8.89^{+0.13}_{-0.13}$	$28.48^{+11.44}_{-5.46}$	$2.07^{+0.50}_{-0.55}$	3.66
SPT0452-50	2.011	$10.07^{+0.13}_{-0.10}$	$19.02^{+2.76}_{-2.34}$	$2.02^{+0.30}_{-0.27}$	1.63
SPT0459-58	4.856	$9.06^{+0.11}_{-0.09}$	$31.52^{+6.78}_{-5.52}$	$2.03^{+0.42}_{-0.37}$	0.68
SPT0459-59	4.799	$9.48^{+0.09}_{-0.09}$	$25.24^{+3.93}_{-2.83}$	$2.29^{+0.30}_{-0.33}$	0.80
SPT0512-59	2.233	$9.39^{+0.04}_{-0.05}$	$29.06^{+1.69}_{-1.46}$	$1.92^{+0.14}_{-0.13}$	0.83
SPT0516-59	3.404	$8.68^{+0.05}_{-0.05}$	$36.36^{+2.21}_{-2.30}$	$1.97^{+0.15}_{-0.13}$	2.31
SPT0520-53	3.779	$9.09^{+0.08}_{-0.07}$	$32.54^{+3.22}_{-4.43}$	$1.83^{+0.27}_{-0.18}$	1.54
SPT0528-53	4.737	$8.69^{+0.12}_{-0.08}$	$36.91^{+6.77}_{-7.38}$	$1.76^{+0.36}_{-0.30}$	1.14
SPT0529-54	3.368	$9.38^{+0.09}_{-0.11}$	$19.07^{+3.29}_{-2.03}$	$2.62^{+0.29}_{-0.36}$	0.80
SPT0532-50	3.399	$9.33^{+0.04}_{-0.04}$	$38.56^{+2.15}_{-1.94}$	$1.38^{+0.13}_{-0.12}$	0.86
SPT0538-50	2.786	$8.98^{+0.05}_{-0.06}$	$33.59^{+1.98}_{-1.75}$	$1.71^{+0.15}_{-0.16}$	1.36
SPT0544-40	4.269	$9.14^{+0.05}_{-0.05}$	$38.11^{+2.45}_{-2.89}$	$1.65^{+0.15}_{-0.14}$	2.75
SPT0550-53	3.128	$9.20^{+0.08}_{-0.09}$	$25.27^{+3.60}_{-2.46}$	$2.17^{+0.26}_{-0.28}$	1.92
SPT0551-48	2.583	$9.54^{+0.06}_{-0.06}$	$39.01^{+2.94}_{-2.66}$	$1.52^{+0.18}_{-0.16}$	2.27
SPT0551-50	3.164	$9.24^{+0.05}_{-0.05}$	$32.99^{+1.71}_{-1.58}$	$1.83^{+0.13}_{-0.12}$	2.83
SPT0552-42	4.438	$9.25^{+0.10}_{-0.09}$	$27.06^{+3.98}_{-3.29}$	$2.03^{+0.25}_{-0.25}$	0.88
SPT0553-50	5.323	$8.89^{+0.07}_{-0.07}$	$39.50^{+5.27}_{-4.90}$	$1.65^{+0.28}_{-0.25}$	0.90
SPT0555-62	4.815	$9.01^{+0.10}_{-0.10}$	$30.00^{+8.01}_{-3.66}$	$2.22^{+0.27}_{-0.40}$	4.84
SPT0604-64	2.481	$9.52^{+0.04}_{-0.04}$	$28.98^{+1.14}_{-1.11}$	$2.13^{+0.09}_{-0.08}$	4.53
SPT0611-55	2.026	$8.92^{+0.07}_{-0.07}$	$19.45^{+1.33}_{-2.26}$	$3.44^{+0.34}_{-0.22}$	4.45

Table B2 – *continued*

Source	Spec-z	$\log[M_{\rm dust}\ (\mathrm{M}_\odot)]$	$T_{\rm dust}$ [K]	β	χ^2_ν
SPT0625-58	2.727	$9.48^{+0.04}_{-0.04}$	$32.41^{+1.44}_{-1.32}$	$1.80^{+0.09}_{-0.09}$	2.85
SPT0652-55	3.347	$9.65^{+0.14}_{-0.08}$	$24.80^{+2.77}_{-4.72}$	$2.35^{+0.39}_{-0.24}$	4.53
SPT2031-51	2.452	$9.40^{+0.04}_{-0.04}$	$29.27^{+1.37}_{-1.26}$	$2.00^{+0.10}_{-0.10}$	2.18
SPT2037-65	3.998	$9.89^{+0.04}_{-0.04}$	$46.72^{+3.06}_{-3.15}$	$0.70^{+0.13}_{-0.11}$	2.16
SPT2048-55	4.090	$9.24^{+0.05}_{-0.06}$	$42.17^{+3.71}_{-3.35}$	$1.11^{+0.15}_{-0.14}$	1.07
SPT2101-60	3.155	$9.11^{+0.04}_{-0.04}$	$33.91^{+1.73}_{-1.70}$	$1.93^{+0.12}_{-0.11}$	1.76
SPT2103-60	4.436	$8.65^{+0.10}_{-0.09}$	$22.20^{+2.88}_{-2.33}$	$2.68^{+0.28}_{-0.29}$	2.44
SPT2129-57	3.260	$9.04^{+0.05}_{-0.05}$	$37.26^{+2.08}_{-1.88}$	$1.75^{+0.11}_{-0.11}$	3.51
SPT2132-58	4.768	$9.24^{+0.09}_{-0.10}$	$29.82^{+9.38}_{-4.40}$	$1.91^{+0.36}_{-0.48}$	1.90
SPT2134-50	2.780	$8.67^{+0.05}_{-0.06}$	$37.39^{+3.60}_{-2.13}$	$1.70^{+0.14}_{-0.15}$	3.51
SPT2146-55	4.567	$9.03^{+0.10}_{-0.10}$	$33.32^{+8.78}_{-5.89}$	$1.80^{+0.39}_{-0.39}$	1.01
SPT2147-50	3.760	$9.01^{+0.07}_{-0.07}$	$30.72^{+3.25}_{-2.49}$	$2.05^{+0.21}_{-0.20}$	2.62
SPT2152-40	3.851	$9.29^{+0.22}_{-0.11}$	$30.11^{+6.51}_{-9.32}$	$1.92^{+0.69}_{-0.38}$	4.47
SPT2203-41	5.194	$9.23^{+0.15}_{-0.12}$	$21.94^{+2.92}_{-2.43}$	$2.84^{+0.24}_{-0.27}$	1.89
SPT2232-61	2.894	$9.18^{+0.06}_{-0.06}$	$27.91^{+2.27}_{-2.59}$	$2.24^{+0.19}_{-0.15}$	2.93
SPT2311-45	2.507	$9.18^{+0.05}_{-0.05}$	$31.51^{+2.45}_{-1.74}$	$1.78^{+0.12}_{-0.14}$	2.71
SPT2311-54	4.280	$9.18^{+0.06}_{-0.06}$	$40.77^{+3.49}_{-4.39}$	$1.83^{+0.20}_{-0.16}$	4.16
SPT2316-50	3.141	$8.71^{+0.13}_{-0.11}$	$23.11^{+3.44}_{-3.33}$	$2.75^{+0.38}_{-0.31}$	1.04
SPT2319-55	5.293	$8.74^{+0.10}_{-0.10}$	$29.34^{+6.12}_{-3.78}$	$2.21^{+0.29}_{-0.33}$	1.10
SPT2332-53	2.726	$9.18^{+0.04}_{-0.05}$	$39.12^{+1.82}_{-1.68}$	$1.86^{+0.11}_{-0.11}$	6.82
SPT2335-53	4.756	$8.46^{+0.11}_{-0.09}$	$30.55^{+4.68}_{-5.40}$	$2.68^{+0.38}_{-0.31}$	1.93
SPT2340-59	3.862	$8.84^{+0.14}_{-0.11}$	$26.28^{+3.79}_{-4.89}$	$2.71^{+0.41}_{-0.29}$	3.62
SPT2349-50	2.876	$9.37^{+0.07}_{-0.07}$	$30.69^{+3.06}_{-4.05}$	$2.06^{+0.24}_{-0.18}$	3.26
SPT2349-52	3.900	$8.58^{+0.22}_{-0.17}$	$19.49^{+4.23}_{-2.99}$	$3.62^{+0.37}_{-0.34}$	2.62
SPT2351-57	5.811	$8.65^{+0.07}_{-0.06}$	$39.58^{+4.69}_{-4.72}$	$1.98^{+0.23}_{-0.21}$	3.76
SPT2353-50	5.578	$8.83^{+0.11}_{-0.10}$	$35.44^{+8.18}_{-6.36}$	$1.94^{+0.37}_{-0.34}$	1.85
SPT2354-58	1.867	$9.09^{+0.05}_{-0.07}$	$31.95^{+3.77}_{-2.00}$	$2.05^{+0.12}_{-0.16}$	1.73
SPT2357-51	3.070	$9.39^{+0.16}_{-0.09}$	$21.63^{+2.26}_{-3.65}$	$2.80^{+0.36}_{-0.24}$	3.82

APPENDIX C: EXAMPLE POSTERIOR DISTRIBUTIONS

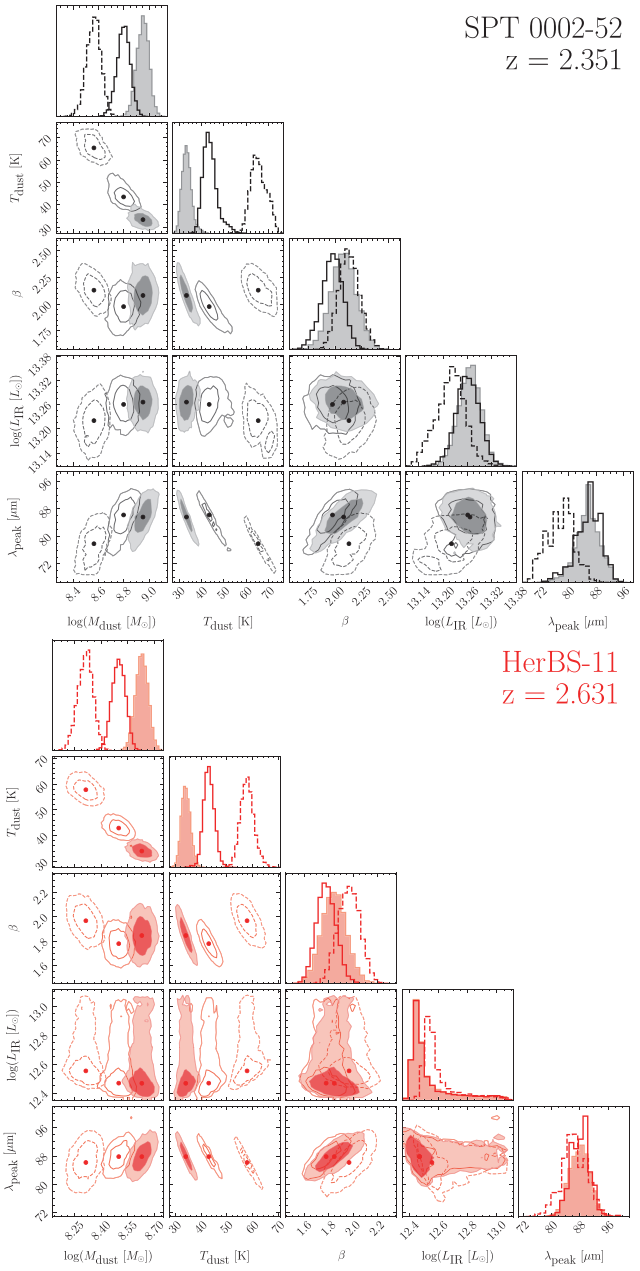

Figure C1. The posterior distributions for SPT 0002-52 and HerBS-11 obtained from FIR SED fitting with an optically thin dust model (shaded contours), and two general opacity models, one with $\lambda_1 = 100$ μm (solid contours), the other with $\lambda_1 = 200$ μm (dashed contours). Parameters shown are the dust mass $M_{\rm dust}$, the dust temperature $T_{\rm dust}$, the dust emissivity index β, IR luminosity $L_{\rm IR}$ and the peak wavelength $\lambda_{\rm peak}$.

This paper has been typeset from a TEX/LATEX file prepared by the author.